Journal of Energy Storage 155 (2026) 121533

Contents lists available at ScienceDirect

Journal of Energy Storage

journal homepage: www.elsevier.com/locate/est

Research papers

Trace additive-induced molecular interface enables highly reversible zinc anodes for aqueous batteries

Xinyu Zhang, Ang Li, Maochun Wu *

Department of Mechanical Engineering, The Hong Kong Polytechnic University, Hung Hom, Kowloon, Hong Kong, China

ARTICLE INFO

Keywords:
Zn metal anode
Self-assembled molecular interface
Electrolyte additive
Rechargeable aqueous Zn batteries
N,N-dimethyl-dithiocarbamylpropyl sulfonic acid sodium salt

ABSTRACT

Zinc (Zn) metal is a highly promising anode material for rechargeable aqueous batteries but suffers from poor reversibility due to dendrite formation and side reactions. Here, we demonstrate that adding trace amounts of *N*, *N*-dimethyl-dithiocarbamylpropyl sulfonic acid sodium salt (DPS) into electrolyte can create a self-assembled molecular interfacial layer to boost the reversibility of Zn anodes. Specifically, the hydrophobic $-N-CH_3$ groups and the zincophilic —S groups anchor the DP^- anions onto Zn anode surface while exposing the hydrophilic $-SO_3^-$ groups to electrolyte. The resulting self-assembled molecular layer not only effectively restricts lateral Zn^{2+} ion diffusion but also facilitates homogeneous interfacial Zn^{2+} ion flux, thereby promoting uniform Zn deposition. Meanwhile, the molecular layer repels H_2O molecules and SO_4^{2-} ions from direct contact with Zn anodes, inhibiting the formation of insulating by-products. As a result, the addition of 0.2 mM DPS enables Zn||Zn symmetric cells to achieve long lifespans of over 3200 h at 2 mA cm^{-2} and 1 mAh cm^{-2} and 785 h at 10 mA cm^{-2} and 10 mAh cm^{-2}. Furthermore, a Zn||MnO_2 full cell using the DPS-modified electrolyte can deliver 194.6 mAh g^{-1} after 600 cycles at 1.0 A g^{-1}, whereas the counterpart cell using pristine $ZnSO_4$ electrolyte short-circuits after 230 cycles. This work provides a facile, cost-effective, and efficient approach to tackling the grand challenges of Zn anodes through the use of trace additives. The proposed strategy is inherently versatile and holds great potential for extension to other rechargeable metal batteries.

1. Introduction

With the rapid increase in the deployment of renewable energy sources such as wind and photovoltaic power, the demand for large-scale energy storage technology is becoming increasingly critical to ensure grid stability [1–4]. Secondary battery energy storage has garnered significant attention for this application due to its high energy density, terrain-independent characteristics, and modular expansion capabilities [5,6]. Compared to widely used lithium-ion batteries, rechargeable aqueous zinc batteries (RAZBs) offer significant promise for large-scale energy storage due to their inherent safety, low cost, and environmental friendliness [7,8]. Moreover, zinc (Zn) metal anode displays a high theoretical volumetric capacity (5855 mAh cm^{-3}) and low electrochemical potential (−0.76 V *vs.* standard hydrogen electrode), ensuring high energy density for practical use. However, Zn metal is thermodynamically unstable in aqueous electrolytes and prone to form dendrites during plating, posing significant challenges to the development of RAZBs [9–11].

To date, numerous strategies have been developed to address the issues with Zn anodes, including electrolyte engineering [12–15], separator modification [16,17], Zn anode structural optimization [18,19] and surface modification [20–22]. Given that Zn stripping/plating and associated side reactions predominantly occur at the Zn anode-electrolyte interface, engineering a stable interface is crucial for enhancing the reversibility of Zn anodes [23]. Coating an artificial layer is one of the most straightforward strategies to regulate the interface. For example, $CaCO_3$ [24], ZnF_2 [25,26] and $ZnSnO_3$ [27] artificial layers have been reported to effectively prevent direct contact between the Zn anode and the electrolyte while guiding the uniform Zn deposition. However, *ex-situ* artificial layers usually suffer from poor adhesion to the Zn anode, particularly under high areal capacities where significant volume change can lead to protective layer detachment from anode surface [28]. An alternative approach is to *in-situ* build a solid electrolyte interphase (SEI) on Zn anode surface by introducing water-in-salt electrolytes [29,30], co-solvent electrolytes [31,32], or eutectic liquids [33,34]. The introduction of high-concentration salts or organic solvents alters the solvation structure of Zn^{2+} ions, which enables Zn^{2+} coordinated organic anions and solvent molecules to decompose preferentially

* Corresponding author.
E-mail address: maochun.wu@polyu.edu.hk (M. Wu).

https://doi.org/10.1016/j.est.2026.121533
Received 6 October 2025; Received in revised form 25 February 2026; Accepted 12 March 2026
Available online 17 March 2026

before Zn deposition, thereby facilitating the *in-situ* formation of SEI on the Zn surface [35]. The *in-situ* formed layer demonstrates good adhesion to Zn anode and exhibits regenerative capability. Additionally, the altered Zn^{2+} solvation structure can reduce the water activity and widen the electrochemical stability window of the electrolyte, consequently suppressing hydrogen evolution reaction (HER) and improving Zn anode reversibility [35,36]. Nevertheless, the *in-situ* strategy typically relies on high-concentration organic solvents or salts, which increase electrolyte viscosity, raise battery costs, and compromise the environmental benefits of aqueous electrolytes.

Here, we propose to introduce a self-assembled molecular interface to simultaneously address the issues of Zn anodes [37–42]. The organic small-molecule additives spontaneously adsorb and enrich on the Zn anode surface even at extremely low concentrations due to specific adsorption affinity for the Zn metal, creating a dynamic adaptive molecular layer that regulates Zn deposition/stripping and mitigates side reactions [43]. This dynamic adaptation of the molecular layer provides sustained protection and regulation of Zn deposition/stripping, avoiding the poor adhesion and mechanical instability observed under high-capacity operation in artificial layers. Moreover, compared to high-concentration electrolyte strategies that require large quantities of salts or organic solvents, this method achieves efficient interface regulation with minimal additive content, preserving the inherent advantages of aqueous electrolytes, such as high safety, cost-effectiveness, and environmental friendliness. As proof of concept, *N*,*N*-dimethyl-dithiocarbamylpropyl sulfonic acid sodium salt (DPS, as shown in Fig. S1) was selected as the functional additive to construct the self-assembled molecular layer at the Zn metal-electrolyte interface. As illustrated in Fig. 1, when added into electrolytes, DPS molecules firmly anchor to Zn surface due to the strong bonding between sulfur atoms in the thiocarbonyl group and Zn metal and the hydrophobicity of $-N-CH_3$ groups, self-forming a molecular layer [44]. Simultaneously, the hydrophilic sulfonate group ($-SO_3^-$) of DPS extends towards the bulk electrolyte. Moreover, the negatively charged $-SO_3^-$ group exhibits strong affinity for cations, thereby capable of regulating Zn^{2+} ion transport at the interface [45,46]. The resulting molecular layer with unique orientation of functional groups not only facilitates homogeneous Zn^{2+} ion flux, thus promoting uniform Zn deposition, but also electrostatically repels SO_4^{2-} anions from participating in side reactions to form insulating $Zn_4SO_4(OH)_6{\cdot}xH_2O$ (ZSH). As a result, the addition of trace amounts of DPS dramatically boosts the reversibility of Zn anodes, enabling a Zn||Zn symmetric cell to achieve remarkable dendrite-free cycling stability exceeding 3200 h at 2 mA cm^{-2} and 1 mAh cm^{-2}. Furthermore, Zn||MnO_2 full cells equipped with DPS-modulated electrolytes can maintain a high discharge specific capacity of 194.6 mAh g^{-1} after 600 cycles at a current density of 1.0 A g^{-1}.

2. Experimental section

2.1. Materials

Zinc sulfate heptahydrate ($ZnSO_4{\cdot}7H_2O$, 99.5 wt%), manganese sulfate ($MnSO_4$, 99.5 wt%), manganese acetate tetrahydrate ($Mn(CH_3COO)_2{\cdot}4H_2O$, 99 wt%), and *N*,*N*-dimethyl-dithiocarbamylpropyl sulfonic acid sodium salt (DPS, 99 wt%) were purchased from Bide. 1-Methyl-2-pyrrolidinone (NMP, 99.9%) and sodium sulfate (Na_2SO_4, 99.0%) were purchased from Aladdin. Zn foil (50 and 100 μm), Cu foil (50 μm), Super P, and polyvinylidene difluoride (PVDF, HSV-900) were purchased from Kejing Co. Ltd.

2.2. Electrolyte preparation

A 2 M (mol L^{-1}) $ZnSO_4$ aqueous electrolyte was prepared by dissolving 0.2 mol of $ZnSO_4{\cdot}7H_2O$ in deionized water to obtain 100 mL of 2 M $ZnSO_4$ aqueous solution (denoted as ZSO) at room temperature. The modified solution was obtained by diluting a concentrated solution. For example, to prepare a ZSO aqueous solution with 0.2 mM DPS (denoted as 0.2DPS/ZSO), the following steps were taken: First, 5 mmol of DPS and 0.2 mol of $ZnSO_4$ were dissolved in deionized water and diluted to 100 mL to obtain a ZSO aqueous solution containing 50 mM DPS. Then,

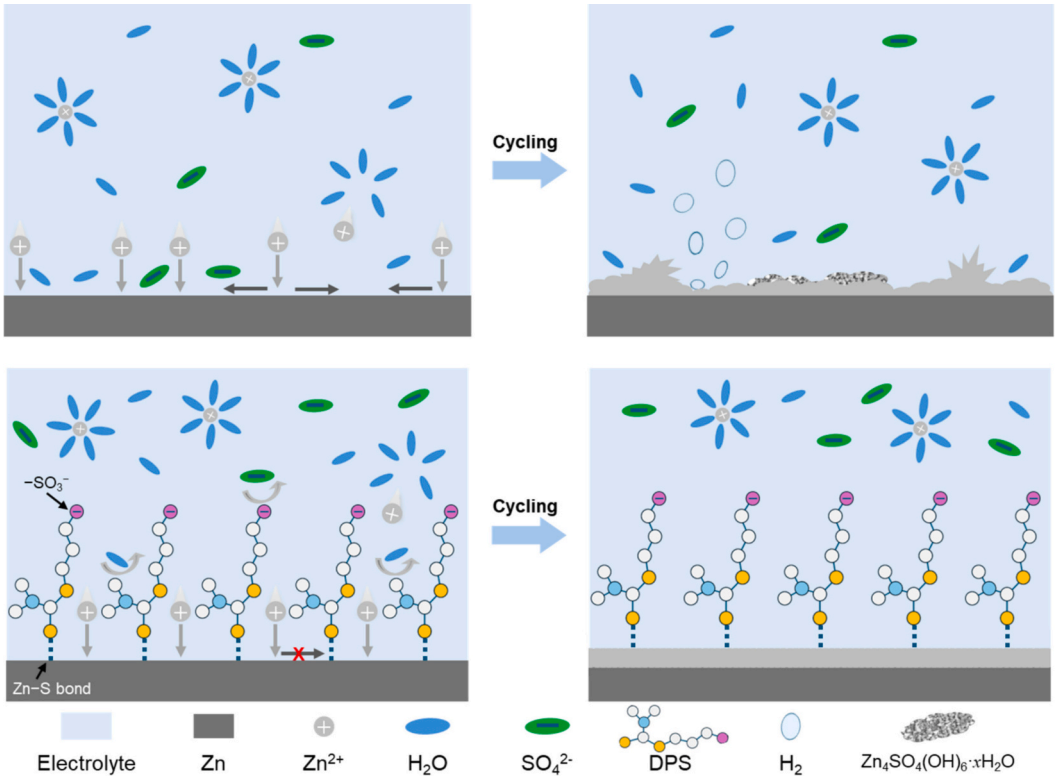

Fig. 1. Schematic illustration of Zn deposition behavior in $ZnSO_4$ electrolytes without (top) and with (bottom) DPS additive.

0.4 mL of the resulting solution was pipetted and mixed with 99.6 mL of the 2 M $ZnSO_4$ aqueous solution to yield 100 mL of 0.2DPS/ZSO aqueous solution. To determine the optimal DPS concentration, a series of ZSO aqueous electrolytes containing 0.1, 0.5, 1, 3, 5, and 10 mM DPS in ZSO were prepared and denoted as 0.1DPS/ZSO, 0.5DPS/ZSO, 1DPS/ZSO, 3DPS/ZSO, 5DPS/ZSO, and 10DPS/ZSO, respectively. All the as-prepared electrolytes remained transparent and clear after standing for 24 h at room temperature, with no visible color change or precipitation.

2.3. Cathode material preparation and cell assembly

For synthesis of α-MnO_2/CNT nanorods [47], a homogeneous dispersion was prepared by adding 0.1000 g of commercial carboxyl-functionalized multi-walled CNTs (diameter $>$ 50 nm, length $<$ 10 μm, purchased from Xianfeng Nano-materials Co., Ltd.) and 0.4865 g of $KMnO_4$ into 60 mL deionized water under magnetic stirring. In parallel, 1.1350 g of $Mn(CH_3COO)_2{\cdot}4H_2O$ was dissolved in 10 mL of deionized water to form a clear solution. The $Mn(CH_3COO)_2$ solution was then introduced dropwise into the preformed dispersion under continuous stirring. The resulting mixture was transferred into a Teflon-lined autoclave and heated at 120 °C for 12 h. After naturally cooling to room temperature, the products were collected by centrifugation, thoroughly washed with deionized water, and dried at 80 °C for 12 h in an electric thermostatic drying oven to obtain the α-MnO_2/CNT nanorods.

For the assembly of coin-type Zn||Zn symmetrical cells, two Zn foils (12 mm diameter) were sandwiched with a GF/D separator (18 mm diameter), with ~80 μL electrolyte added. For Zn||Cu cells, Zn foils (12 mm diameter) served as anodes while Cu foils (12 mm diameter) as cathodes. The α-MnO_2 cathodes were fabricated as follows: α-MnO_2/CNT nanorods, carbon black, and PVDF with a mass ratio of 7:2:1 were dry-mixed for 0.5 h, then blended with NMP to form a homogeneous slurry. The slurry was uniformly coated onto a carbon paper using a doctor blade, dried at 80 °C, and punched into 12-mm discs (~2 mg cm^{-2} α-MnO_2 loading). Finally, coin-type Zn||MnO_2 full cells were assembled using these cathodes and 12-mm-diameter Zn anodes. Additionally, commercial activated carbon (AC, Kuraray Co., Ltd.) was used directly as the active material for hybrid supercapacitors without further treatment. Cathodes with AC were prepared using the same mass ratio (7:2:1 of AC/carbon black/PVDF), achieving an active material loading of ~3 mg cm^{-2}.

2.4. Material characterizations and electrochemical measurements

The material surface morphology was observed using a field-emission scanning electron microscope (FE-SEM, TESCAN VEGA3), while *in-situ* optical observations were performed with a stereo microscope (Olympus SZ61TR). Crystal structure analysis was conducted *via* X-ray diffraction (XRD, Rigaku SmartLab) with Cu Kα radiation (λ = 1.5406 Å) at 45 kV. Fourier-transform infrared spectroscopy (FTIR, Thermo Fisher Scientific iN10) was employed to examine the solvation structure of Zn^{2+} ions in aqueous electrolyte. The adsorption behavior of DPS on Zn anode surface was investigated by X-Ray photoelectron spectroscopy (XPS, Thermo Fisher Scientific Nexsa) equipped with Al Kα X-ray source.

Electrochemical measurements, including potentiodynamic polarization test, cyclic voltammetry (CV), electrochemical impedance spectroscopy (EIS), chronoamperometry (CA), linear sweep voltammetry (LSV), and differential capacitance analysis, were performed using a Biologic VSP-3e electrochemical workstation. Galvanostatic charge/discharge cycling and rate capability tests were performed using a Neware battery testing system. Tafel curves were acquired in the potential range of −0.20 to +0.20 V (*vs.* open-circuit potential) at a scan rate of 0.5 mV s^{-1}. CV measurements employed Zn||Cu coin cells between −0.2 and + 0.6 V (*vs.* Zn/Zn^{2+}) at 5 mV s^{-1}. EIS spectra were recorded from 1 MHz to 0.01 Hz with an AC amplitude of 10 mV. CA tests were conducted on Zn||Zn symmetric cells under a constant potential of −150 mV for 500 s. LSV measurements were performed at a scan rate of 1.0 mV s^{-1} using a three-electrode configuration, with Zn foil as the working electrode, Pt mesh as the counter electrode, and Ag/AgCl as the reference electrode. Differential capacitance was evaluated using Zn||Cu asymmetric cells at an AC frequency of 1 kHz with an amplitude of 5 mV.

2.5. Density functional theory (DFT) calculations

DFT calculations were implemented by employing the ABINIT code [48]. The projector augmented wave (PAW) method was employed to describe the core electrons. The Zn(002) surface was constructed using a three-layer 6 × 6 supercell. The convergence criteria for energy and force in geometry optimizations were set to 4×10^{-5} Ha $Bohr^{-1}$ and 4×10^{-4} Ha $Bohr^{-1}$, respectively. The custom energy cutoff was 22 Ha. The adsorption energy (E_{abs}) between the Zn metal and different molecules (DP^- and water) was calculated by using the following formula:

$$E_{abs} = E_{total} - E_{Zn} - E_{H2O/DP} - \quad (1)$$

where E_{total}, E_{Zn}, and $E_{H2O/DPS}$ are the energies of the whole system, the Zn metal anode, and the H_2O or DP^-, respectively.

To optimize molecular structure, DFT calculations were performed using the ORCA program (version 5.0). All calculated structures were optimized using the ωB97XD/def2-TZVP level of theory and analyzed by Multiwfn software. The implicit solvation model (water) was adopted. By analyzing the highest occupied molecular orbital (HOMO) and the lowest unoccupied molecular orbital (LUMO), the electrochemical properties of the different reactants were derived.

3. Results and discussion

To elucidate the effects of DPS additive on the performance of Zn electrodes, a series of theoretical calculations, electrochemical measurements, and material characterizations were conducted. First, DFT calculations were performed to gain insights into the molecular interaction between Zn anode and DPS additive. As displayed in Fig. 2a, the adsorption energy of DP^- on Zn surface is −4.01 eV, which is far more negative than that of H_2O (−0.27 eV), indicating that DP^- will be preferentially adsorbed on Zn surface. The DP^- also exhibits remarkably more negative adsorption energies compared to those of the H_2O, irrespective of the crystal plane orientation. It indicates the preferential adsorption of DP^- onto the Zn surface, as shown in Fig.S2. Moreover, it is found that there is an apparent overlapped electron density between Zn and S atoms of DP^-. This result suggests that the strong affinity between DP^- and Zn is mainly governed by the Zn—S interaction. Fig. 2b presents the energy levels of the LUMO and HOMO of H_2O and DP^-. Compared to H_2O, DP^- has a lower energy of LUMO (−0.92 eV *vs.* 2.41 eV) and a higher energy of HOMO (−5.59 eV *vs.* −8.10 eV), indicating stronger electron transfer propensity between DP^- and Zn metal, and thus a higher tendency of DP^- adsorption onto Zn surface [14]. The interaction between different species at the Zn anode-electrolyte interface was also computed by DFT calculations. Results in Fig. 2c show that Zn^{2+}−DP^- exhibits a more negative binding energy (−66.57 kcal mol^{-1}) than that of Zn^{2+}–H_2O (−26.20 kcal mol^{-1}), indicating that Zn^{2+} prefers to coordinate with DP^- ion, which facilitates the transfer of Zn^{2+} ions at the interface. Furthermore, the binding energy of H_2O−H_2O (−5.50 kcal mol^{-1}) is lower compared to that of H_2O−DP^- (−40.89 kcal mol^{-1}). Thus, the adsorbed DP^- ion can disrupt the hydrogen-bond network of H_2O at the Zn anode-electrolyte interface, which can reduce the side reactions on the Zn anode surface [41]. In addition, the minimum electrostatic potential (ESP) of water and DP^- ion was calculated and presented in Fig. S3. It can be seen that DP^- ion exhibits a lower ESP than water, with its negative charge primarily localized

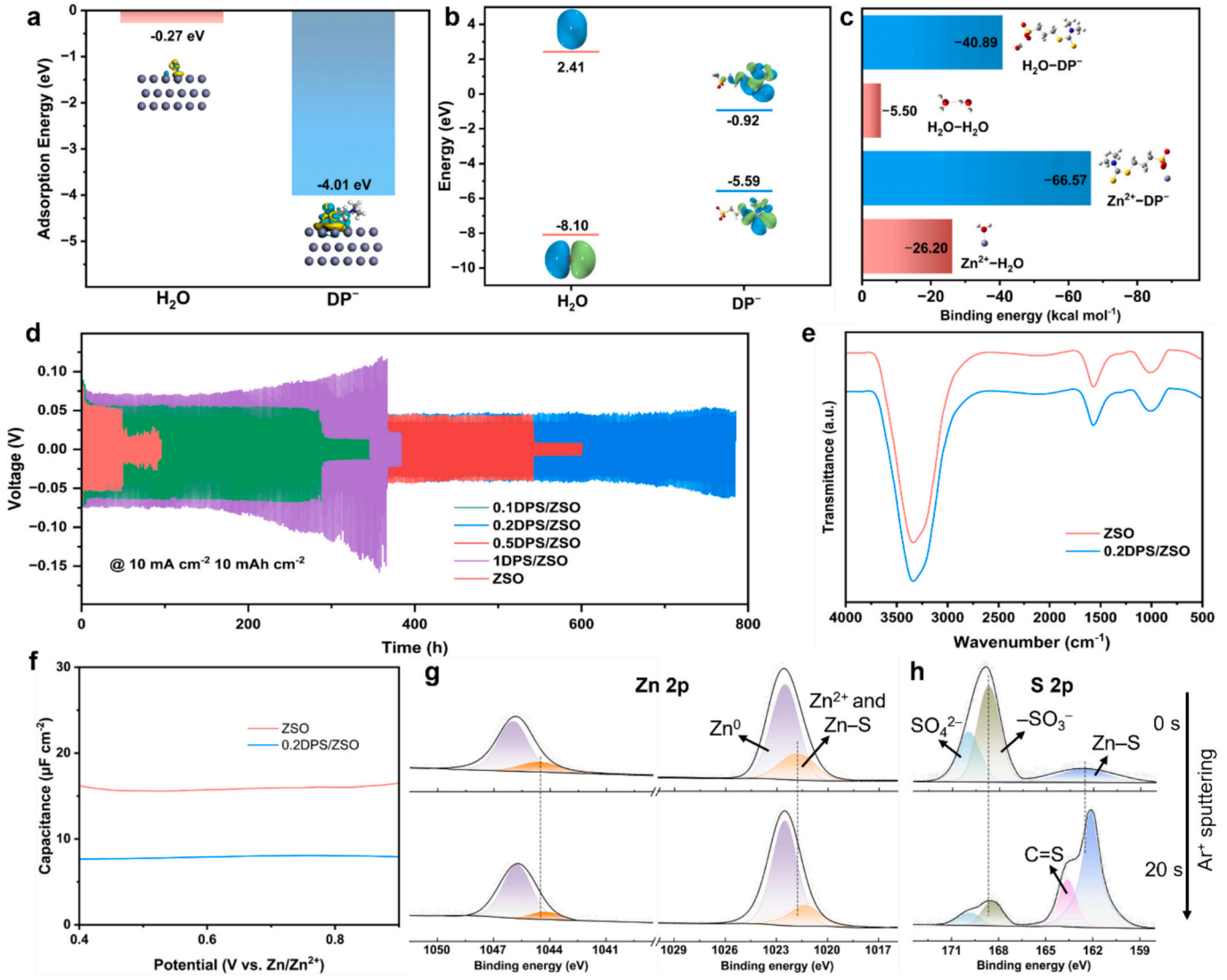

Fig. 2. (a) Adsorption energy of H_2O and DP^- on the Zn(002) facet. (b) Frontier molecular orbital energy of H_2O and DP^-. (c) Binding energies of Zn^{2+}−H_2O, Zn^{2+}−DP^-, H_2O−H_2O, and H_2O−DP^-. (d) Long-term cycling tests of Zn||Zn symmetric cells with different electrolytes at 10 mA cm^{-2} with an areal capacity of 10 mAh cm^{-2}. (e) FT-IR spectra of ZSO and 0.2DPS/ZSO electrolytes. (f) Differential capacitance curves in ZSO and 0.2DPS/ZSO electrolytes. Depth-profiling XPS spectra of (g) Zn 2p and (h) S 2p for Zn foil after immersion in 0.2DPS/ZSO electrolyte for 24 h.

around the $-SO_3^-$ group. Therefore, it can be inferred that the preferential adsorption of DP^- ions on Zn anode surface can form a strong negatively charged shield layer, which effectively repels SO_4^{2-} ions, thereby fundamentally suppressing the formation of ZSH byproducts [49].

The preceding DFT results indicate that DP^- can adsorb onto the Zn anode surface, forming a self-assembled layer that regulates Zn^{2+} ion transport and deposition. It can be envisioned that the concentration of DP^- will impose a significant effect on the properties of the electrode-electrolyte interface, thereby impacting the behavior of Zn plating and stripping. To identify the optimal concentration of DPS additive, we assembled various Zn||Zn symmetric cells with the as-prepared electrolytes, including ZSO, 0.1DPS/ZSO, 0.2DPS/ZSO, 0.5DPS/ZSO, 1DPS/ZSO, 3DPS/ZSO, 5DPS/ZSO, 10DPS/ZSO, and 50DPS/ZSO, and cycled them at 10 mA cm^{-2} with an areal capacity of 10 mAh cm^{-2}. As shown in Figs. 2d and S4, cells with pure ZSO electrolyte short-circuit within 48 h, whereas all DPS-added electrolytes significantly extend the cycle life of Zn||Zn symmetric cells. Notably, 0.2DPS/ZSO electrolyte shows the best performance, enabling the Zn||Zn symmetric cell to achieve a lifespan of 785 h, which is over 16 times longer than that of the cells with pristine electrolyte. Therefore, 0.2DPS/ZSO was chosen for subsequent investigations.

FT-IR spectroscopy was then acquired to investigate the properties of the bulk electrolyte. Results in Fig. 2e show that the peaks corresponding to the O−H stretching vibration (3362 and 3230 cm^{-1}), the O−H bending vibration (1639 cm^{-1}), and the SO_4^{2-} vibration (1091 cm^{-1}) remain unchanged after adding 0.2 mM DPS, indicating that the introduction of DPS additive does not alter the solvation structure of Zn^{2+} in the bulk electrolyte. The adsorption behavior of DPS on the surface of Zn anode was examined using EIS tests at different potentials. As shown in Fig. 2f, the addition of DPS reduces the capacitance within the scanned potential range, suggesting its preferential adsorption on the surface of Zn metal [50]. XPS depth profiling was further performed to investigate the interaction between the additive and Zn anode. The peak located at 1021.2 eV in the Zn 2p spectra (Fig. 2g) confirms the formation of c with adsorbed Zn^{2+} species [37]. A small shift in this peak is observed after sputtering, possibly due to the removal of Zn^{2+} ions adsorbed on the outer layer and thereby exposing the Zn—S bond. The S 2p spectra (Fig. 2h) show that the peaks of $-SO_x^-$ species and Zn-thiol groups exhibit opposite gradients with increasing sputtering depth, where the $-SO_3^-$ groups are mainly enriched on the outer surface of the interface, while the Zn-thiol groups are anchored on the inner surface [44]. Meanwhile,

a new peak corresponding to the C═S bond at 163.6 eV appears after sputtering [51], implying that the C═S bond in the DPS is located at the inner surface of the self-assembled interface layer. In the C 1s spectra (Fig. S5), the slight peak at 285.7 eV corresponds to the C—N species before sputtering [37]. This peak becomes more obvious after sputtering, which indicates that the −N−CH_3 groups of DPS are located at the bottom of the molecular interface layer. Based on the above analysis of the XPS spectra at different sputtering depths, it can be determined that a DPS monolayer is constructed on the surface of Zn anode through the Zn—S bond formed between DPS and Zn anode. FT-IR was also employed to probe the interaction between DPS and Zn anode. As shown in Fig. S6, the pronounced peaks between 650 and 850 cm^{-1} were assigned to the Zn—S stretching [52,53], indicating that DPS and the Zn anode can interact *via* Zn—S (thiol) bond. To further evaluate the stability of DPS during long-term cycling, the Zn anode surface after cycling was analyzed by XPS (Figs. S7–S8). Notably, even after 200 cycles, DPS-derived components remain detectable on the Zn surface, indicating that DPS can persist at the Zn/electrolyte interface during long-term operation.

The effects of the DPS on the electrochemical performance of Zn anodes were then examined by different techniques. First, the nucleation overpotentials of Zn anode in different electrolytes were probed by the chronopotential method. As shown in Fig. 3a, the nucleation overpotential of the Zn anode in the electrolyte with 0.2DPS/ZSO (48 mV) is significantly lower than that in the ZSO electrolyte (72.8 mV), which may be attributed to the more negative binding energy of DP^- adsorbed on the Zn anode surface with Zn^{2+}, thus accelerating Zn^{2+} transfer. A lower nucleation overpotential favors more homogeneous and dense nuclei, which is beneficial for subsequent (002) facet growth [54]. To elucidate the impact of DPS additive on the Zn nucleation and growth, CA tests were performed by applying a constant potential of −150 mV to the Zn||Zn symmetric cells. Notably, the current density–time profile in CA provides a sensitive indicator of the change of the electrochemically active surface area of the Zn anode during electrodeposition. As shown in Fig. 3b, the current response in the ZSO electrolyte increases continuously throughout the CA test, indicating a continuous increase in the true surface area of Zn anode. This behavior is closely associated with non-uniform Zn deposition. During the nucleation stage on a bare Zn surface, the adsorbed Zn^{2+} ions tend to diffuse laterally across the electrode surface and preferentially aggregate into initial nuclei to minimize surface energy and exposed area. Subsequently, the locally concentrated electric field around these nascent protuberances (the "tip effect") further attracts Zn^{2+} ions and drives their continuous lateral diffusion, thereby amplifying these initial nuclei into severe dendrites, as illustrated in the lower inset of Fig. 3b [54]. This phenomenon confirms the non-uniform Zn deposition behavior in the ZSO electrolyte. In contrast, the cell with 0.2DPS/ZSO electrolyte only exhibits a rapid increase in current within the first 100 s, followed by a stable current plateau. This result suggests that the Zn anode surface area remains constant during plating in the presence of DPS additive. The dramatic change in deposition behavior induced by the DPS additive can be understood as follows. The adsorption of DP^- at the Zn surface can form a strong negatively charged shield layer and facilitate the transfer of Zn^{2+} ions at the interface, which provides more uniformly distributed nucleation sites. Consequently, the arriving Zn^{2+} ions are compelled to deposit at these abundant sites in proximity to their initial adsorption points, rather than undergoing lateral diffusion to the protrusions, as shown in the upper inset of Fig. 3b. This process leads to significantly increased nucleation density, thereby promoting uniform and planar deposition [55].

To better understand how the DPS-induced self-assembled molecular interface affects Zn electrodeposition, an *in-situ* optical microscopy system was constructed to monitor real-time morphological evolution of the Zn electrode during plating. As illustrated in Fig. 3c, significant protrusions emerge on the Zn surface after plating for 30 min at 10 mA cm^{-2} in ZSO electrolyte. These Zn protrusions result in locally concentrated electric field that triggers preferential Zn^{2+} ion accumulation and reduction, which is known as the "tip effect" and is responsible for dendrite proliferation. In contrast, the Zn electrode surface remains flat and dense after plating for 60 min at 10 mA cm^{-2} in 0.2DPS/ZSO electrolyte (Fig. 3d), demonstrating the effective regulation of Zn migration and deposition by the DPS self-assembled molecular interface. To further verify the effectiveness of the DPS additive in inhibiting dendrite formation during cycling, we systematically examined the

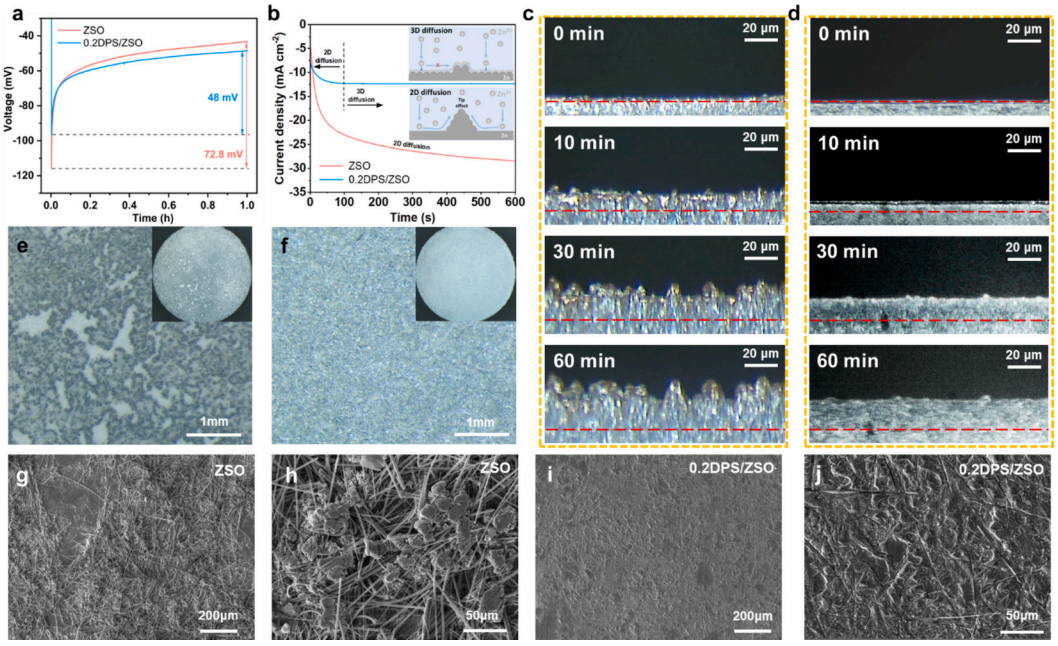

Fig. 3. (a) Initial Zn nucleation overpotential in Zn||Zn symmetric cells at 2 mA cm^{-2} with different electrolytes. (b) CA curves of Zn||Zn symmetric cells in two electrolytes under an overpotential of −150 mV. *In-situ* optical microscopy observations of Zn deposition at a current density of 10 mA cm^{-2} in (c) ZSO and (d) 0.2DPS/ZSO electrolytes. The optical images of Zn anodes after 20 cycles in (e) ZSO and (f) 0.2DPS/ZSO electrolytes at 10 mA cm^{-2} and 10 mAh cm^{-2}. SEM images of cycled Zn anode surface after 20 cycles at 10 mA cm^{-2} and 10 mAh cm^{-2} in Zn||Zn symmetric cells using (g, h) ZSO and (i, j) 0.2DPS/ZSO electrolytes.

morphology of cycled Zn metal anodes at various current densities and areal capacities by optical microscopy and SEM. Fig. 3e presents an optical micrograph of a Zn anode cycled for 20 cycles in ZSO electrolyte at 10 mA cm^{-2} and 10 mAh cm^{-2}. The Zn electrodeposits exhibit significant morphological non-uniformity, with certain regions showing minimal or no deposition. In contrast, the Zn anode cycled in the 0.2DPS/ZSO electrolyte exhibits a uniform and dense surface (Fig. 3f). SEM images (Figs. 3g, h and S9a, b) corresponding to the Zn anode in Fig. 3e reveal numerous Zn dendritic protrusions formed during cycling, which grow into the glass fiber separator and cause puncture damage. Conversely, SEM images of the Zn anode cycled in the 0.2DPS/ZSO electrolyte (Figs. 3i, j and S9c, d) show a smooth surface without notable protrusions and only a few deposits on the glass fibers. A similar phenomenon was consistently observed at other current densities and areal capacities (Fig. S10). These optical microscopy and SEM observations demonstrate the critical role of the DPS molecular interface in promoting uniform Zn deposition.

To examine the capability of DPS self-assembled molecular interface in suppressing side reactions, we conducted a series of electrochemical measurements. First, LSV tests in a three-electrode system were deployed to evaluate the suppression of HER by DPS. To preclude interference from Zn^{2+} reduction, 1 M Na_2SO_4 solution was used in place of $ZnSO_4$ electrolyte. As shown in Fig. 4a, the current response in the 0.2DPS/Na_2SO_4 electrolyte was markedly lower within the HER potential window than that in pure Na_2SO_4 electrolyte, confirming that DPS effectively inhibits water decomposition. This is primarily attributed to the DPS layer at the interface that blocks direct contact between water molecules and the electrode [44,56]. Tafel polarization measurements were conducted to assess the corrosion resistance of the Zn anode in the two electrolytes (Fig. 4b). Upon addition of DPS, the corrosion current density decreased from 24.24 to 8.47 mA cm^{-2}. The markedly reduced corrosion rate demonstrates that DPS significantly enhances the corrosion resistance of Zn electrodes. The corrosion behavior of Zn anode was further investigated through EIS tests on Zn||Zn symmetric cells after a 2-day rest. As shown in Fig. 4c, Nyquist plots of both electrolytes show two capacitive semicircles, indicating the formation of corrosion product film on Zn anodes. The high-frequency semicircle corresponds to charge transfer resistance (R_{ct}), while the low-frequency one reflects film impedance (R_{film}) [57]. The EIS were fitted with ZSimpWin software using the equivalent circuit model R(QR)(QR) inserted in Fig. 4c. Results show that the corrosion product film resistance of Zn anode soaked in 0.2DPS/ZSO (596.5 Ω) is considerably lower than that soaked in ZSO (1595 Ω), proving that DPS can effectively suppress the formation of Zn corrosion product.

Morphologies of Zn foils after 10 days of immersion in the electrolytes were characterized by SEM. Compared to pristine Zn (Fig. S11a and b), ZSH corrosion products form on the Zn foil surface in both electrolytes (Fig. 4d and e). Nevertheless, the entire surface of Zn foils immersed in ZSO electrolyte is covered with flaky corrosion products, with localized agglomerations observed in some regions (Figs. 4d and S11c), whereas the surface of Zn foil soaked in 0.2DPS/ZSO displays only sparsely distributed, fine corrosion products (Figs. 4e and S11d). XRD was then performed to characterize the composition of corrosion products. As displayed in Fig. 4f, the addition of DPS significantly reduces the diffraction peak intensity of the ZSH byproduct, further validating its capability in mitigating Zn corrosion. To evaluate the corrosion-inhibiting effect of the DPS additive during cycling, we performed XRD measurements on Zn foils harvested from symmetric cells after cycling at 2 mA cm^{-2} and 1 mA h cm^{-2} in the ZSO electrolyte (100 cycles) and the 0.2DPS/ZSO electrolyte (200 cycles). The results are shown in Fig. S9. The Zn anode cycled in ZSO exhibits distinct diffraction peaks attributable to corrosion by-products [58–60], whereas these characteristic peaks are greatly weakened (nearly suppressed) for the Zn anode cycled in 0.2DPS/ZSO, even after a longer cycling period. This comparison demonstrates that DPS effectively enhances the corrosion resistance of the Zn anode during prolonged cycling. Furthermore, Raman mapping was employed to evaluate the spatial distribution of corrosion by-products on the cycled Zn anode surfaces, and the results are shown in Fig. S10. As presented in Fig. S10a, the Zn anode cycled in the baseline electrolyte exhibits distinct Raman peaks at 1152, 1110, 1011, and 967 cm^{-1}, which can be assigned to $Zn_4SO_4(OH)_6{\cdot}xH_2O$, indicating substantial accumulation of sulfate-based corrosion products. In contrast, for the Zn anode cycled in the 0.2DPS/ZSO electrolyte, these characteristic peaks are much less pronounced, and their overall

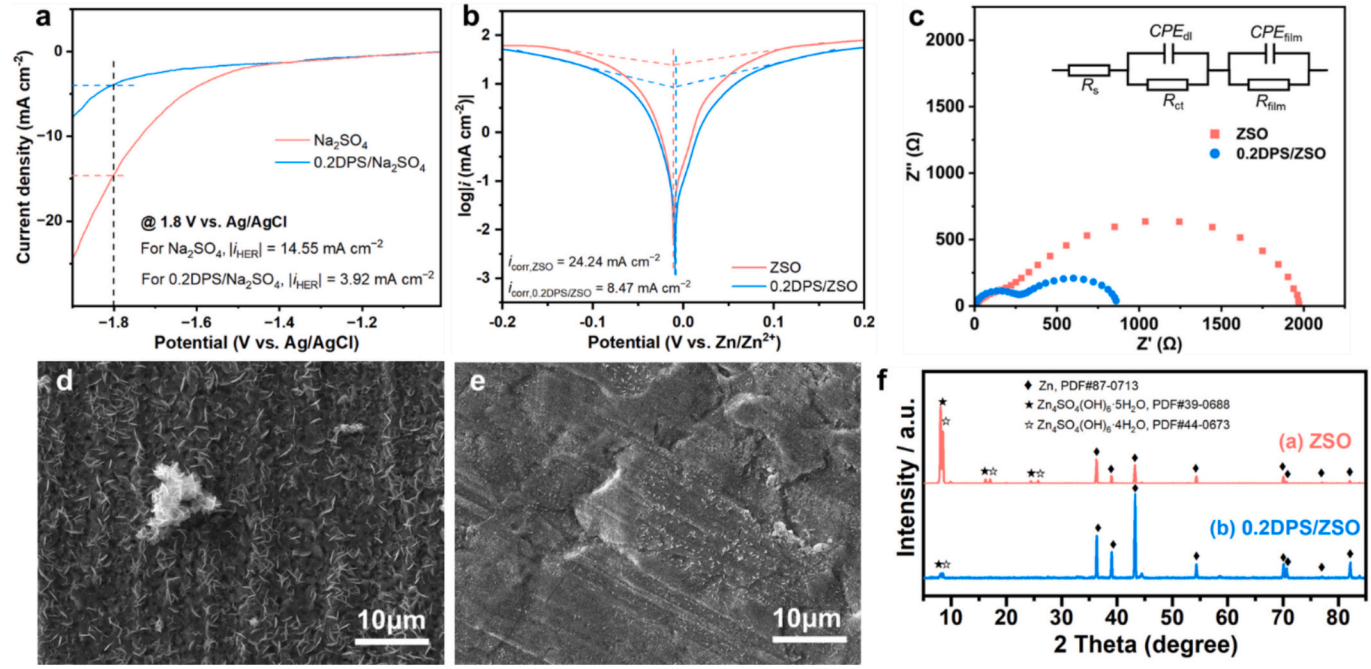

Fig. 4. (a) LSV curves in Na_2SO_4 electrolytes with and without DPS additive. (b) Tafel plots of Zn anodes measured in ZSO and 0.2DPS/ZSO electrolytes. (c) Nyquist plots of Zn||Zn symmetric cells with ZSO and 0.2DPS/ZSO electrolytes after resting for 48 h. SEM images of Zn foils soaked in the (d) ZSO and (e) 0.2DPS/ZSO electrolytes for 10 days. (f) XRD patterns of Zn foils soaked in ZSO and 0.2DPS/ZSO electrolytes for 10 days.

intensity is significantly reduced, suggesting markedly suppressed by-product formation. To further visualize the by-product distribution, the dominant band at 967 cm^{-1} was selected for Raman mapping. Raman mapping over a 40 μm × 40 μm area (Fig. S10b and S10c) reveals a much lower signal level for the Zn anode cycled in 0.2DPS/ZSO, with count values ranging from 315 to 335. This intensity is approximately one order of magnitude lower than that of the Zn anode cycled in the ZSO electrolyte (counts: 3265–3285), confirming that DPS effectively reduces the amount of corrosion by-product accumulation on the Zn surface [61,62].

Cycling stability of Zn||Zn symmetric cells is a key metric for assessing the efficacy of electrolyte additives. To this end, symmetric cells with different electrolytes were assembled and subject to long-term cycling at various current densities and areal capacities. As shown in Fig. 5a, the symmetric cell using ZSO electrolyte short-circuits after only 101 h at 2 mA cm^{-2} and 1 mAh cm^{-2}, indicating its poor cycling stability. In stark contrast, the cell assembled with 0.2DPS/ZSO electrolyte demonstrates an exceptional cycling lifespan of more than 3230 h (32 times longer than that of the control group) while maintaining a low overpotential of approximately 34 mV throughout the test. This remarkable improvement is ascribed to the efficient suppression of Zn dendrite growth and side reactions by the DPS additive. Notably, the beneficial effect of DPS on the anode performance was retained even under demanding conditions. As shown in Fig. S7, the addition of 0.2 mM DPS dramatically extends the cycle life of the symmetric cell from 67 to 910 h at 5 mA cm^{-2} and 5 mAh cm^{-2}. Even under harsher conditions with an ultra-high current density and areal capacity (20 mA cm^{-2} and 20 mAh cm^{-2}), the symmetric cell with 0.2DPS/ZSO electrolyte can still operate for 212 h, whereas the control group cell fails after only 37 h (Fig. 5b). Table S1 [14,63–66] compares the performance of this work with recently reported. It can be seen that the DPS additive outshines most of the reported additives under various operating conditions, demonstrating the superiority of the proposed strategy in addressing the challenges of Zn electrodes.

To further substantiate the practical applicability of trace DPS additive, we assembled Zn||Zn symmetric cells using a thin Zn foil (50 μm thick) for high depth-of-discharge (DOD) cycling tests. As presented in Fig. S8, the cells using the designed electrolyte display cycle lifespans of 140, 102, and 92 h when cycled at 10 mA cm^{-2} with DODs of 60%, 70%, and 80%, respectively. Additionally, the rate capability of Zn||Zn symmetric cells with two different electrolytes was assessed by fixing the areal capacity of 1 mAh cm^{-2} and stepwise increasing the current density from 1 to 40 mA cm^{-2}, after which it was decreased back to 1 mA cm^{-2}. As shown in Fig. 5c, the symmetric cells using both electrolytes operate normally during the initial rate cycling test stage. However, the symmetric cell with the ZSO electrolyte suffers from short

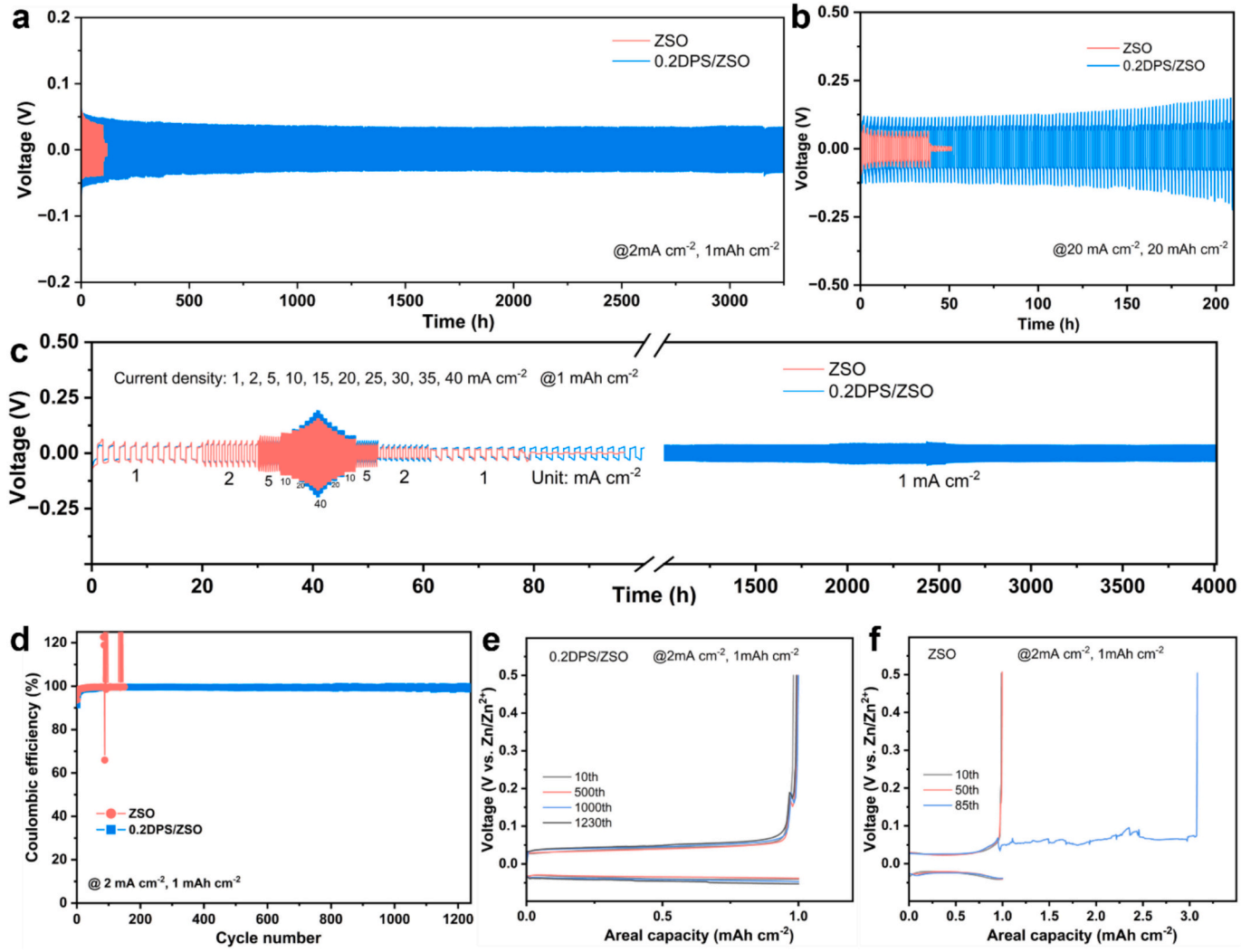

Fig. 5. Long-term galvanostatic cycling performance of Zn||Zn symmetric cells with ZSO and 0.2DPS/ZSO electrolytes at (a) 2 mA cm^{-2} and 1 mAh cm^{-2} and (b) 20 mA cm^{-2} and 20 mAh cm^{-2}. (c) Comparison of the rate capability of Zn||Zn symmetric cells with different electrolytes. (d) CEs of Zn||Cu asymmetric cells using ZSO and 0.2DPS/ZSO electrolytes and (e, f) corresponding charge and discharge curves.

circuits after several cycles when the current density returns to 1 mA cm^{-2}. In contrast, the symmetric cell using 0.2DPS/ZSO electrolyte continues to cycle stably for more than 4000 h without short-circuit and maintains a low overpotential of ~23 mV. These results demonstrate that the additive-induced self-assembled molecular layer can adapt to various-rate operations, which continuously suppresses Zn dendrite growth and side reactions. In contrast, conventional electrolyte fails to suppress dendrite growth under high current density, leading to a premature short-circuit-induced failure during subsequent galvanostatic cycling.

Zn||Cu asymmetric cells were further used to evaluate the reversibility of Zn plating/stripping at 2 mA cm^{-2} and 1 mAh cm^{-2}. As shown in Fig. 5d, the cell with DPS-added electrolyte achieves a long cycle life surpassing 1230 h with an average Coulombic efficiency (CE) of up to 99.45%, whereas the additive-free control group fails rapidly only after 83 h and exhibits a lower average CE of 99.16% before failure. Furthermore, the voltage-capacity curves (Fig. 5e) reveal smooth, highly overlapping plating/stripping curves for the cell with DPS-containing electrolyte, corroborating its excellent reversibility. In contrast, due to a short circuit at the 85th cycle, the asymmetric cell with ZSO electrolyte required over 0.5 h to reach the cutoff potential during Zn stripping from the Cu electrode (Fig. 5f). To further investigate the underlying reasons for the extended life of Zn cells, Zn deposits on Cu substrates were examined by SEM. Without the DPS additive, the electrodeposited Zn was unevenly distributed and entangled with glass fiber separator (Figs. S9a and b), which led to low CE and premature failure. In contrast, as shown in Figs. S9c and d, the DPS-containing electrolyte produced uniform, dense, fine-grained Zn deposition layers. These observations confirm that the DPS additive is crucial for achieving homogeneous Zn deposition.

To evaluate the versatile practicality of the proposed additive, we assembled Zn||MnO_2 full cells and Zn||AC hybrid supercapacitors using different electrolytes. For the Zn||MnO_2 full cells, 0.1 M $MnSO_4$ solution was added to both ZSO and 0.2DPS/ZSO electrolytes to mitigate the

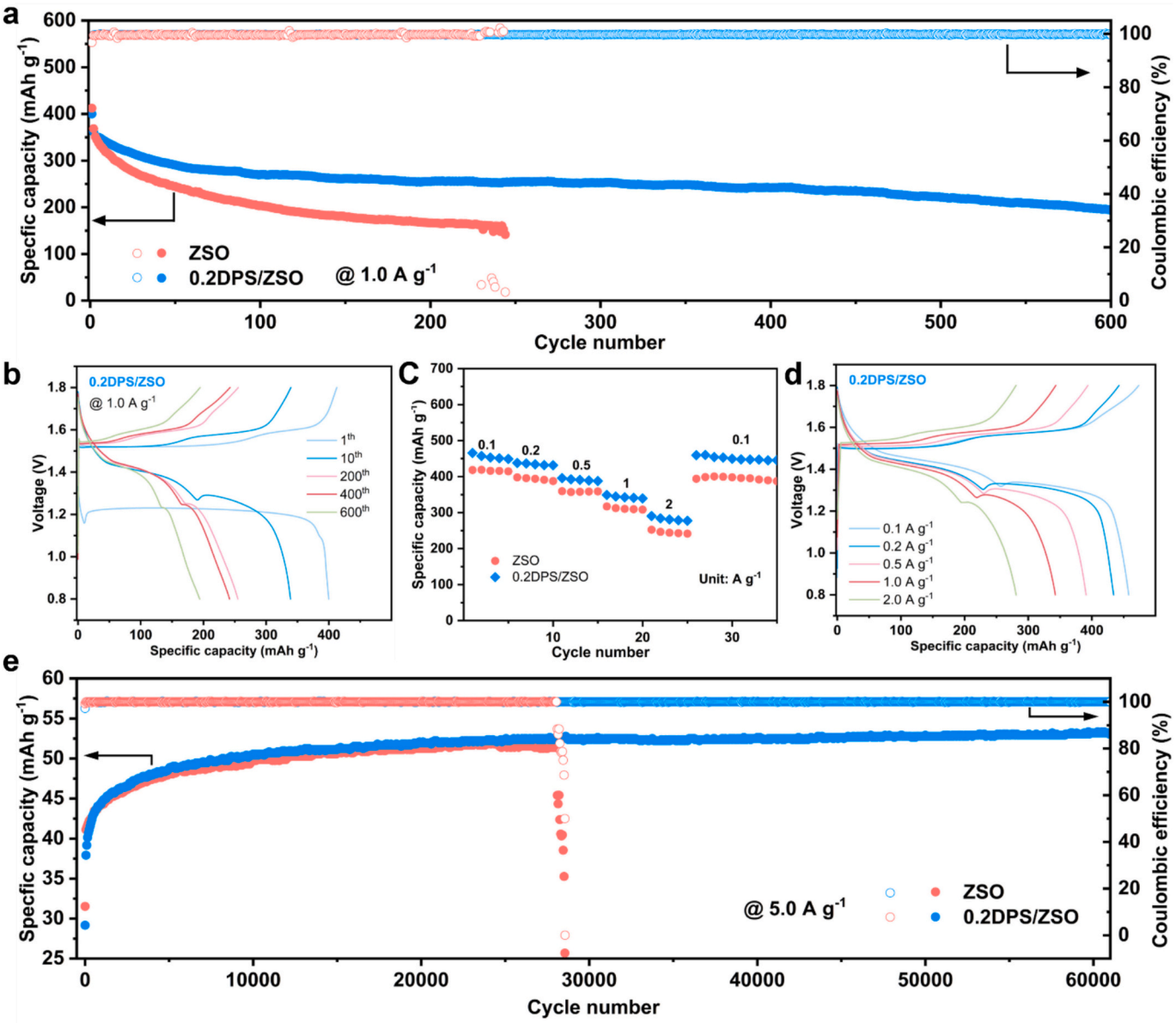

Fig. 6. (a) Long-term cycling performance of Zn||MnO_2 full cells with/without DPS additive at a current density of 1.0 A g^{-1} and (b) the corresponding voltage-capacity curves of the Zn||MnO_2 full cell with DPS additive. (c) Rate capability of Zn||MnO_2 full cells with/without DPS additive at various current densities, and (d) the corresponding voltage-capacity curves of the Zn||MnO_2 full cell with DPS additive. (e) Long-term cycling performance of Zn||AC hybrid supercapacitors with/without DPS additive at a current density of 5.0 A g^{-1}.

dissolution of MnO_2 cathode [67]. Long-term cycling tests were conducted at a current density of 1.0 A g^{-1} (~2 mA cm^{-2}). As shown in Fig. 6a and b, both cells deliver comparable initial discharge specific capacities (412 mAh g^{-1} for the cell using the ZSO electrolyte and 399 mAh g^{-1} for the cell using the DPS-added electrolyte) and suffer from significant capacity decay in the second cycle. Such early-cycle capacity fading has been widely reported for MnO_2-based aqueous Zn batteries and is generally attributed to an irreversible structural transformation during the initial Zn^{2+} intercalation into MnO_2 [67,68]. However, the capacity of the full cell with ZSO electrolyte continues to drop rapidly and suffers from short-circuit-induced failure after 230 cycles. The short cycle life primarily results from continuous Zn dendrite growth in ZSO electrolyte, which is consistent with the cycling behavior of Zn||Zn symmetric cells. In contrast, the Zn||MnO_2 full cell assembled with 0.2DPS/ZSO electrolyte exhibits a much slower capacity decay rate. Even after 600 cycles, it retains a specific capacity of 194.6 mAh g^{-1}, which again confirms the effectiveness of DPS additive in boosting the reversibility of Zn electrodes. Table S2 [14,69,70] compares the performance of this work with recently reported. It can be seen that the DPS additive outshines most of the reported additives in terms of capacity retention ratio, demonstrating the superiority of the proposed strategy in addressing the challenges of Zn||MnO_2 cells. Moreover, rate capability was evaluated at various current densities (0.1, 0.2, 0.5, 1.0, and 2.0 A g^{-1}), and the results are displayed in Fig. 6c and d. It is found that the cell using 0.2DPS/ZSO electrolyte delivers higher specific capacity than that with pristine electrolyte under all tested currents (Fig. 6c). More specifically, the full cell equipped with 0.2DPS/ZSO electrolyte delivers average specific capacities of 455, 434, 391, 343, and 282 mAh g^{-1}, respectively, in comparison to 416, 393, 358, 311, and 245 mAh g^{-1} for the cell with blank electrolyte. Furthermore, Fig. 6e shows that the use of 0.2DPS/ZSO electrolyte enables the Zn-AC supercapacitor to stably cycle over 60,000 cycles at 5 A g^{-1} (corresponding to ~15 mA cm^{-2}). Conversely, the supercapacitor with ZSO electrolyte fails after 28,000 cycles due to Zn dendrite-induced short circuits. These results underscore the substantial potential of the 0.2DPS/ZSO electrolyte for practical applications.

4. Conclusion

In summary, a trace amount of DPS additives was introduced into RAZBs to construct a unique molecular interfacial layer to boost the reversibility of Zn anodes. Theoretical calculations and experimental characterizations reveal that the hydrophobic $-N-CH_3$ groups and the zincophilic —S groups render the preferential adsorption of DP^- anions, forming an interface layer with negatively charged $-SO_3^-$ groups exposed to the electrolyte. The uniquely tailored interface effectively regulates the uniform Zn deposition and suppresses side reactions. As a result, the DPS-added electrolytes considerably extend the cycle life of Zn anodes. Markedly, in the presence of 0.2 mM DPS, a Zn||Zn symmetric cell can cycle 785 h even under harsh conditions of 10 mA cm^{-2} and 10 mAh cm^{-2}. Furthermore, the DPS-added electrolyte enables a Zn||MnO_2 full cell to retain a high specific capacity of 194.6 mAh g^{-1} after 600 cycles at 1.0 A g^{-1}. These encouraging results demonstrate that trace-additive-induced self-assembled molecular interface offers a simple and effective strategy to improve the reversibility of Zn anodes, thereby paving the way for the development of long-life RAZBs.

CRediT authorship contribution statement

Xinyu Zhang: Writing – review & editing, Writing – original draft, Visualization, Validation, Methodology, Investigation, Formal analysis, Data curation, Conceptualization. **Ang Li:** Writing – review & editing, Visualization, Software, Data curation. **Maochun Wu:** Writing – review & editing, Supervision, Resources, Project administration, Funding acquisition.

Declaration of competing interest

The authors declare that they have no known competing financial interests or personal relationships that could have appeared to influence the work reported in this paper.

Acknowledgements

The work described in this paper was supported by the grants from the Research Grants Council of the Hong Kong Special Administrative Region, China (Project No. 16205822) and PolyU Start-up Fund (Project No. 1-BDC4).

Appendix A. Supplementary data

Supplementary data to this article can be found online at https://doi.org/10.1016/j.est.2026.121533.

Data availability

Data will be made available on request.

References

[1] Z.X. Zhu, T.L. Jiang, M. Ali, Y.H. Meng, Y. Jin, Y. Cui, W. Chen, Rechargeable batteries for grid scale energy storage, Chem. Rev. 122 (22) (2022) 16610–16751, https://doi.org/10.1021/acs.chemrev.2c00289.
[2] Z.H. Yu, X.J. Jia, Y.H. Cai, R.H. Su, Q. Zhu, T.S. Zhao, H.R. Jiang, Electrolyte engineering for efficient and stable vanadium redox flow batteries, Energy Storage Mater. 69 (2024), https://doi.org/10.1016/j.ensm.2024.103404.
[3] Y. Luo, J.L. Shen, H.W. Liang, L. Sun, L. Dong, Supporting building life cycle carbon monitoring, reporting and verification: a traceable and immutable blockchain-empowered information management system and application in Hong Kong, Resour. Conserv. Recycl. 208 (2024), https://doi.org/10.1016/j.resconrec.2024.107736.
[4] H. Iqbal, S. Sarwar, D. Kirli, J.K.H. Shek, A.E. Kiprakis, A survey of second-life batteries based on techno-economic perspective and applications-based analysis, Carbon Neutrality 2 (1) (2023) 8, https://doi.org/10.1007/s43979-023-00049-5.
[5] Y.M. Huang, J. Li, Key challenges for grid-scale lithium-ion battery energy storage, Adv. Energy Mater. 12 (48) (2022), https://doi.org/10.1002/aenm.202202197.
[6] J. Sun, Z. Guo, L. Pan, X. Fan, L. Wei, T. Zhao, Redox flow batteries and their stack-scale flow fields, Carbon Neutrality 2 (1) (2023) 30.
[7] H.P. Wang, R. Tan, Z.X. Yang, Y.Z. Feng, X.C. Duan, J.M. Ma, Stabilization perspective on metal anodes for aqueous batteries, Adv. Energy Mater. 11 (2) (2021), https://doi.org/10.1007/s43979-023-00072-6.
[8] X.X. Jia, C.F. Liu, Z.G. Neale, J.H. Yang, G.Z. Cao, Active materials for aqueous zinc ion batteries: synthesis, crystal structure, morphology, and electrochemistry, Chem. Rev. 120 (15) (2020) 7795–7866, https://doi.org/10.1021/acs.chemrev.9b00628.
[9] A. Li, J.Y. Li, Y.R. He, M.C. Wu, Toward stable and highly reversible zinc anodes for aqueous batteries via electrolyte engineering, J. Energy Chem. 83 (2023) 209–228, https://doi.org/10.1016/j.jechem.2023.04.006.
[10] Q. Yang, Q. Li, Z.X. Liu, D.H. Wang, Y. Guo, X.L. Li, Y.C. Tang, H.F. Li, B.B. Dong, C.Y. Zhi, Dendrites in Zn-based batteries, Adv. Mater. 32 (48) (2020), https://doi.org/10.1002/adma.202001854.
[11] Y.Y. Wang, Z.J. Wang, W.K. Pang, W. Lie, J.A. Yuwono, G.M. Liang, S.L. Liu, A. M. D' Angelo, J.J. Deng, Y.M. Fan, K. Davey, B.H. Li, Z.P. Guo, Solvent control of water O-H bonds for highly reversible zinc ion batteries, Nat. Commun. 14 (1) (2023), https://doi.org/10.1038/s41467-023-38384-x.
[12] Z. Tian, H. Liu, M. Cheng, L. Cui, R. Zhang, X. Yang, D. Wu, D. Wang, J. Xia, Ethanol as solvent additives with competitive effect for high-stable aqueous zinc batteries, ACS Appl. Mater. Interfaces 16 (17) (2024) 21857–21867, https://doi.org/10.1021/acsami.4c01484.
[13] S.D. Zhang, Q.Z. Gou, W.G. Chen, H.R. Luo, R.D. Yuan, K.X. Wang, K.D. Hu, Z. Y. Wang, C.D. Wang, R.Q. Liu, Z.X. Zhang, Y. Lei, Y.J. Zheng, L. Wang, F. Wan, B. Y. Li, M. Li, Co-regulating solvation structure and hydrogen bond network via bio-inspired additive for highly reversible zinc anode, Adv. Sci. 11 (35) (2024), https://doi.org/10.1002/advs.202404968.
[14] A. Li, X. Zhang, Z. Xu, M. Wu, Non-sacrificial additive regulated electrode–electrolyte interface enables long-life, deeply rechargeable aqueous Zn anodes, Chem. Eng. J. 494 (2024) 153240, https://doi.org/10.1016/j.cej.2024.153240.
[15] A. Li, Z. Xu, X. Zhang, M. Wu, Cation and anion co-modulated electrolytes enable highly textured and reversible zinc anodes for durable aqueous batteries, J. Energy Chem. 106 (2025) 688–698, https://doi.org/10.1016/j.jechem.2025.03.010.
[16] Y.C. Liang, D.T. Ma, N. Zhao, Y.Y. Wang, M. Yang, J.B. Ruan, G.H. Yang, H.W. Mi, C.X. He, P.X. Zhang, Novel concept of separator design: efficient ions transport modulator enabled by dual-interface engineering toward ultra-stable Zn metal

anodes, Adv. Funct. Mater. 32 (25) (2022), https://doi.org/10.1002/adfm.202112936.
[17] Y.C. Tan, D. Chen, T.Y. Yao, Y.M. Zhang, C.L. Miao, H. Yang, Y.H. Wang, L. Li, V. Kotsiubynskyi, W. Han, L.F. Shen, Tailoring Zn flux by an ion acceleration layer modified separator for high-rate long-lasting Zn metal anodes, Adv. Sci. 11 (44) (2024), https://doi.org/10.1002/advs.202407410.
[18] Y. Zeng, Z. Pei, D. Luan, X.W.D. Lou, Atomically dispersed zincophilic sites in N,P-codoped carbon macroporous fibers enable efficient Zn metal anodes, J. Am. Chem. Soc. 145 (22) (2023) 12333–12341, https://doi.org/10.1021/jacs.3c03030.
[19] Y. Mu, Z. Li, B.-k. Wu, H. Huang, F. Wu, Y. Chu, L. Zou, M. Yang, J. He, L. Ye, M. Han, T. Zhao, L. Zeng, 3D hierarchical graphene matrices enable stable Zn anodes for aqueous Zn batteries, Nat. Commun. 14 (1) (2023) 4205, https://doi.org/10.1038/s41467-023-39947-8.
[20] L.R. Feng, A. Li, J.K. Zhang, J.Y. Xie, M.C. Wu, B.L. Su, X.H. Guo, Customizing Helmholtz plane with N, F, P tri-doped rGO/CNT aerogel protective layer for long-life zinc-ion batteries, Small Methods 9 (8) (2025), https://doi.org/10.1002/smtd.202500066.
[21] S. Zhang, J. Chen, W. Chen, Y. Su, Q. Gou, R. Yuan, Z. Wang, K. Wang, W. Zhang, X. Hu, Z. Zhang, P. Wang, F. Wan, J. Liu, B. Li, Y. Wang, G. Zheng, M. Li, J. Sun, Regulating water molecules via bioinspired covalent organic framework membranes for Zn metal anodes, Angew. Chem. Int. Ed. 137 (14) (2025) e202424184, https://doi.org/10.1002/ange.202424184.
[22] M. Tang, Q. Liu, X. Zou, Z. Yu, K. Zhang, B. Zhang, L. An, Engineering in situ heterometallic layer for robust Zn electrochemistry in extreme $Zn(BF_4)_2$ electrolyte environment, Energy Storage Mater. 74 (2025) 103896, https://doi.org/10.1016/j.ensm.2024.103896.
[23] J. Zhang, Y. Wang, Z. Zhao, P. Li, G. Tang, W. Chen, Z. Peng, Unveiling the descriptor of parasitic reactions of zinc anode: a comparative study of trace pyridinesulfonic acid-based additives in aqueous electrolyte, Adv. Energy Mater. 14 (34) (2024) 2401560, https://doi.org/10.1002/aenm.202401560.
[24] L.T. Kang, M.W. Cui, F.Y. Jiang, Y.F. Gao, H.J. Luo, J.J. Liu, W. Liang, C.Y. Zhi, Nanoporous $CaCO_3$ coatings enabled uniform Zn stripping/plating for long-life zinc rechargeable aqueous batteries, Adv. Energy Mater. 8 (25) (2018), https://doi.org/10.1002/aenm.201801090.
[25] J. Han, H. Euchner, M. Kuenzel, S.M. Hosseini, A. Gross, A. Varzi, S. Passerini, A thin and uniform fluoride-based artificial interphase for the zinc metal anode enabling reversible Zn/MnO_2 batteries, ACS Energy Lett. 6 (9) (2021) 3063–3071, https://doi.org/10.1021/acsenergylett.1c01249.
[26] L. Ma, Q. Li, Y. Ying, F. Ma, S. Chen, Y. Li, H. Huang, C. Zhi, Toward practical high-areal-capacity aqueous zinc-metal batteries: quantifying hydrogen evolution and a solid-ion conductor for stable zinc anodes, Adv. Mater. 33 (12) (2021) 2007406, https://doi.org/10.1002/adma.202007406.
[27] F.X. Ling, L.F. Wang, F.F. Liu, M.Z. Ma, S.P. Zhang, X.H. Rui, Y. Shao, Y.X. Yang, S. N. He, H.G. Pan, X.J. Wu, Y. Yao, Y. Yu, Multi-scale structure engineering of $ZnSnO_3$ for ultra-long-life aqueous zinc-metal batteries, Adv. Mater. 35 (23) (2023), https://doi.org/10.1002/adma.202208764.
[28] X.H. Zeng, J.F. Mao, J.N. Hao, J.T. Liu, S.L. Liu, Z.J. Wang, Y.Y. Wang, S.L. Zhang, T. Zheng, J.W. Liu, P.H. Rao, Z.P. Guo, Electrolyte design for in situ construction of highly Zn-conductive solid electrolyte interphase to enable high-performance aqueous Zn-ion batteries under practical conditions, Adv. Mater. 33 (11) (2021), https://doi.org/10.1002/adma.202007416.
[29] F. Wang, O. Borodin, T. Gao, X. Fan, W. Sun, F. Han, A. Faraone, J.A. Dura, K. Xu, C. Wang, Highly reversible zinc metal anode for aqueous batteries, Nat. Mater. 17 (6) (2018) 543–549, https://doi.org/10.1038/s41563-018-0063-z.
[30] Y. Zhang, G. Wan, N.H.C. Lewis, J. Mars, S.E. Bone, H.-G. Steinrück, M. R. Lukatskaya, N.J. Weadock, M. Bajdich, O. Borodin, A. Tokmakoff, M.F. Toney, E. J. Maginn, Water or anion? Uncovering the Zn^{2+} solvation environment in mixed $Zn(TFSI)_2$ and LiTFSI water-in-salt electrolytes, ACS Energy Lett. 6 (10) (2021) 3458–3463, https://doi.org/10.1021/acsenergylett.1c01624.
[31] F. Ming, Y. Zhu, G. Huang, A.-H. Emwas, H. Liang, Y. Cui, H.N. Alshareef, Co-solvent electrolyte engineering for stable anode-free zinc metal batteries, J. Am. Chem. Soc. 144 (16) (2022) 7160–7170.
[32] J. Heo, D. Dong, Z. Wang, F. Chen, C. Wang, Electrolyte design for aqueous Zn batteries, Joule 9 (4) (2025) 101844, https://doi.org/10.1021/jacs.1c12764.
[33] J. Jiang, Y. Chen, Y. Li, Z. Ju, G. Yang, J. Wang, S. Kumar, S.Y. Tee, G. Yu, Z. W. Seh, Regulating Zn^{2+} solvation structure in eutectic electrolytes for rechargeable zinc batteries, Matter 8 (2) (2025) 101917, https://doi.org/10.1016/j.matt.2024.11.011.
[34] L. Geng, J. Meng, X. Wang, C. Han, K. Han, Z. Xiao, M. Huang, P. Xu, L. Zhang, L. Zhou, L. Mai, Eutectic electrolyte with unique solvation structure for high-performance zinc-ion batteries, Angew. Chem. Int. Ed. 62 (22) (2023), https://doi.org/10.1002/anie.202303744.
[35] X. Li, X. Wang, L. Ma, W. Huang, Solvation structures in aqueous metal-ion batteries, Adv. Energy Mater. 12 (37) (2022) 2202068, https://doi.org/10.1002/aenm.202202068.
[36] Y.X. Song, X.J. Chen, J. Wang, K. Wang, Y.H. Zhang, L.X. Zhang, X.B. Zhong, J. F. Liang, R. Wen, Highly reversible Zn anodes enabled by in-situ construction of zincophilic zinc polyacrylate interphase for aqueous Zn-ion batteries, J. Colloid Interface Sci. 678 (2025) 284–291, https://doi.org/10.1016/j.jcis.2024.08.178.
[37] Z. Wei, S. Wang, D. Li, S. Yang, S. Guo, G. Qu, Y. Yang, H. Li, Surface charge-reinforced and ion-selective layers for stable metal zinc anode chemistry, Energy Environ. Sci. 17 (15) (2024) 5440–5450, https://doi.org/10.1039/D4EE01260G.
[38] B. Ren, S. Hu, A. Chen, X. Zhang, H. Wei, J. Jiang, G. Chen, C. Zhi, H. Li, Z. Liu, Inhibiting dendrite formation and electrode corrosion via a scalable self-assembled mercaptan layer for stable aqueous zinc batteries, Adv. Energy Mater. 14 (3) (2024) 2302970, https://doi.org/10.1002/aenm.202302970.
[39] S. Wang, S. Wang, Z. Wei, Y. Wang, D. Zhang, Z. Chen, C. Zhi, A parts-per-million scale electrolyte additive for durable aqueous zinc batteries, Nat. Commun. 16 (1) (2025) 1800, https://doi.org/10.1038/s41467-025-56607-1.
[40] H. Li, Y. Gan, J. Zeng, M. Lv, B. Shang, W. Li, Unveiling the mechanism of ultra-low-dose and ultra-high corrosion inhibition additive for enhancing zinc anode performance, Corros. Sci. 224 (2023) 111544, https://doi.org/10.1016/j.corsci.2023.111544.
[41] G. Duan, Y. Wang, L. Sun, Z. Bao, B. Luo, S. Zheng, Z. Ye, J. Huang, Y. Lu, Atomic pinning of trace additives induces interfacial solvation for highly reversible Zn metal anodes, ACS Nano 17 (22) (2023) 22722–22732, https://doi.org/10.1021/acsnano.3c07257.
[42] Y.X. Song, X.F. Wang, C.B. Liu, K.X. Guo, X.H. Guo, X.B. Zhong, Y.H. Zhang, K. Wang, H.J. Guo, L.X. Zhang, J.F. Liang, A widely used nonionic surfactant with desired functional groups as aqueous electrolyte additives for stabilizing Zn anode, Rare Metals 43 (8) (2024) 3692–3701, https://doi.org/10.1007/s12598-024-02754-1.
[43] Y.X. Song, J. Wang, X.B. Zhong, K. Wang, Y.H. Zhang, H.T. Liu, L.X. Zhang, J. F. Liang, R. Wen, Interfacial chemistry regulation via dibenzenesulfonamide-functionalized additives enables high-performance Zn metal anodes, Energy Storage Mater. 58 (2023) 85–93, https://doi.org/10.1016/j.ensm.2023.03.005.
[44] H. Gan, H. Li, M. Xu, C. Han, H.-M. Cheng, Failure mechanisms and remedy of an ultrathin Zn metal anode in pouch cells, Joule 8 (11) (2024) 3054–3071, https://doi.org/10.1016/j.joule.2024.07.013.
[45] W.J. Zhou, K. Bao, H. Chen, F. Liu, X. Zhang, W.A. Daoud, Synergistic surface adsorption and pH regulation enable highly reversible zinc metal anodes, Chem. Eng. J. 517 (2025), https://doi.org/10.1016/j.cej.2025.164267.
[46] W.J. Zhou, M. Yang, M.F. Chen, G.F. Zhang, X. Han, J.Z. Chen, D.T. Ma, P. X. Zhang, Ion-sieving effect enabled by sulfonation of cellulose separator realizing dendrite-free Zn deposition, Adv. Funct. Mater. 34 (27) (2024), https://doi.org/10.1002/adfm.202315444.
[47] Q. Jian, T. Wang, J. Sun, M. Wu, T. Zhao, In-situ construction of fluorinated solid-electrolyte interphase for highly reversible zinc anodes, Energy Storage Mater. 53 (2022) 559–568, https://doi.org/10.1016/j.ensm.2022.08.033.
[48] H.R. Jiang, W. Shyy, L. Zeng, R.H. Zhang, T.S. Zhao, Highly efficient and ultra-stable boron-doped graphite felt electrodes for vanadium redox flow batteries, J. Mater. Chem. A 6 (27) (2018) 13244–13253, https://doi.org/10.1039/C8TA03388A.
[49] G. Duan, Y. Wang, B. Luo, L. Sun, S. Zheng, J. Huang, Z. Ye, Taurine-mediated dynamic bridging strategy for highly stable Zn metal anode, Energy Storage Mater. 61 (2023) 102882, https://doi.org/10.1016/j.ensm.2023.102882.
[50] Y. Wang, L.e. Mo, X. Zhang, Y. Ren, T. Wei, Z. Li, Y. Huang, H. Zhang, G. Cao, L. Hu, Facet-termination promoted uniform Zn (100) deposition for high-stable zinc-ion batteries, Adv. Energy Mater. 13 (31) (2023) 2301517, https://doi.org/10.1002/aenm.202301517.
[51] H. Qin, W. Kuang, N. Hu, X. Zhong, D. Huang, F. Shen, Z. Wei, Y. Huang, J. Xu, H. He, Building metal-molecule interface towards stable and reversible Zn metal anodes for aqueous rechargeable zinc batteries, Adv. Funct. Mater. 32 (47) (2022) 2206695, https://doi.org/10.1002/adfm.202206695.
[52] D. Li, Y. Tang, S. Liang, B. Lu, G. Chen, J. Zhou, Self-assembled multilayers direct a buffer interphase for long-life aqueous zinc-ion batteries, Energy Environ. Sci. 16 (8) (2023) 3381–3390, https://doi.org/10.1039/D3EE01098H.
[53] R. Yemini, S. Blanga, H. Aviv, I. Perelshtein, E. Teblum, S. Dery, E. Gross, Y. Mastai, M. Noked, O. Lidor-Shalev, Growth of hybrid chiral thin films by molecular layer deposition zinc/cysteine as a case study, Adv. Mater. Interfaces 9 (3) (2022) 2101725, https://doi.org/10.1002/admi.202101725.
[54] Y. Lin, Z. Mai, H. Liang, Y. Li, G. Yang, C. Wang, Dendrite-free Zn anode enabled by anionic surfactant-induced horizontal growth for highly-stable aqueous Zn-ion pouch cells, Energy Environ. Sci. 16 (2) (2023) 687–697, https://doi.org/10.1039/D2EE03528F.
[55] Z. Yang, C. Lv, W. Li, T. Wu, Q. Zhang, Y. Tang, M. Shao, H. Wang, Revealing the two-dimensional surface diffusion mechanism for zinc dendrite formation on zinc anode, Small 18 (43) (2022) 2104148, https://doi.org/10.1002/smll.202104148.
[56] Y. Lv, M. Zhao, Y. Du, Y. Kang, Y. Xiao, S. Chen, Engineering a self-adaptive electric double layer on both electrodes for high-performance zinc metal batteries, Energy Environ. Sci. 15 (11) (2022) 4748–4760, https://doi.org/10.1039/D2EE02687B.
[57] M. Mouanga, P. Berçot, Comparison of corrosion behaviour of zinc in NaCl and in NaOH solutions; part II: electrochemical analyses, Corros. Sci. 52 (12) (2010) 3993–4000, https://doi.org/10.1016/j.corsci.2010.08.018.
[58] J.Y. Peng, W.H. Song, W. Zhang, X.Y. Li, Q. Ma, B. Wu, M. Fujishige, K. Takeuchi, M. Endo, C.D. Ji, Y.L. Sun, J. Niu, F. Wang, Bone-inspired sustainable hydrogel electrolytes for Zn metal batteries, Angew. Chem. Int. Ed. 64 (34) (2025), https://doi.org/10.1002/anie.202506449.
[59] W.H. Song, L.Q. Ye, J.Y. Peng, Q. Ma, B. Wu, B.Y. Jiang, M. Fujishige, K. Takeuchi, M. Endo, C.D. Ji, J. Niu, F. Wang, Enabling high-performance Zn anodes through nitrogen-participated p-π conjugation in hydrogel electrolytes, Adv. Energy Mater. 15 (36) (2025), https://doi.org/10.1002/aenm.202503484.
[60] Q. Ma, W.H. Song, B. Wu, C.J. Zheng, M. Fujishige, K. Takeuchi, M. Endo, J. Niu, F. Wang, Insight into the Zn-salt anion effects on polysaccharide-containing electrolytes for Zn anode modifications, Energy Storage Mater. 80 (2025), https://doi.org/10.1016/j.ensm.2025.104388.
[61] W. Song, B. Jiang, Y. Wang, Q. Ma, B. Wu, L. Ye, J. Xu, M. Fujishige, K. Takeuchi, M. Endo, J. Niu, F. Wang, Building powerful zinc-ion hybrid capacitors by an energy drink-inspired strategy, Small 21 (14) (2025) 2412842, https://doi.org/10.1002/smll.202412842.

[62] Z. Zhao, R. Wang, C. Peng, W. Chen, T. Wu, B. Hu, W. Weng, Y. Yao, J. Zeng, Z. Chen, P. Liu, Y. Liu, G. Li, J. Guo, H. Lu, Z. Guo, Horizontally arranged zinc platelet electrodeposits modulated by fluorinated covalent organic framework film for high-rate and durable aqueous zinc ion batteries, Nat. Commun. 12 (1) (2021) 6606, https://doi.org/10.1038/s41467-021-26947-9.

[63] X. Hu, Z. He, Q. Zhao, J. Zhou, C. Wang, S. Huang, G. Zhou, B. Xu, B. Wang, L. Chen, Y. Chen, Adaptive no-tip distribution of rich charge-density-clusters guiding confinement deposition with repair function toward highly reversible zinc anode, Adv. Funct. Mater. 34 (49) (2024) 2409247, https://doi.org/10.1002/adfm.202409247.

[64] W. Liu, Q. Zhao, R. Jiang, X. Ni, T. You, C. Li, Y. Deng, B. Xu, Y. Chen, L. Chen, Stereoisomeric engineering mediated zinc metal electrodeposition: critical balance of solvation and adsorption capability, Adv. Powder Mater. 4 (2) (2025) 100276, https://doi.org/10.1002/adfm.202409247.

[65] A. Li, Z.Y. Xu, S.W. Lo, X.Y. Zhang, H.R. Jiang, M.C. Wu, Kinesin-mimetic ion director enables highly oriented Zn deposition in aqueous batteries, Adv. Funct. Mater. (2025), https://doi.org/10.1002/adfm.202518964.

[66] T.Q. Wu, C. Hu, Q. Zhang, Z.F. Yang, G.H. Jin, Y.X. Li, Y.G. Tang, H.H. Li, H. Y. Wang, Helmholtz plane reconfiguration enables robust zinc metal anode in aqueous zinc-ion batteries, Adv. Funct. Mater. 34 (30) (2024), https://doi.org/10.1002/adfm.202315716.

[67] Y. Liao, H.-C. Chen, C. Yang, R. Liu, Z. Peng, H. Cao, K. Wang, Unveiling performance evolution mechanisms of MnO_2 polymorphs for durable aqueous zinc-ion batteries, Energy Storage Mater. 44 (2022) 508–516, https://doi.org/10.1016/j.ensm.2021.10.039.

[68] H. Chen, C. Dai, F. Xiao, Q. Yang, S. Cai, M. Xu, H.J. Fan, S.J. Bao, Reunderstanding the reaction mechanism of aqueous Zn–Mn batteries with sulfate electrolytes: role of the zinc sulfate hydroxide, Adv. Mater. 34 (15) (2022) 2109092, https://doi.org/10.1002/adma.202109092.

[69] S.A. Zheng, Y. Wang, B. Luo, L.L. Sun, G.S. Duan, J.Y. Huang, Z.Z. Ye, In-situ formation of heterogeneous interfaces inducing surface crystallographic manipulation toward highly stable Zn anode, Chem. Eng. J. 473 (2023), https://doi.org/10.1016/j.cej.2023.145313.

[70] Z.X. Cao, X.F. Ma, W.X. Liu, J.R. Wu, Y.J. Jiao, Y.H. Yin, Z.S. Lu, S.T. Yang, Simultaneous modulation on solvation shell and electrode interface for reversible zinc anode realized by a mutiplefunctional additive, Adv. Funct. Mater. 35 (6) (2025), https://doi.org/10.1002/adfm.202414956.